machines

MDPI

Article

Prediction of Slurry Erosion–Corrosion in SLM-Produced Ti-6Al-4V Using ANFIS Modeling: Influence of Impact Angles and Erodent Mass

Saleh Ahmed Aldahash [1,*], Ibrahem Maher [2,3], Yasser Abdelrhman [1,4] and Osama Abdelaal [1,4]

[1] Department of Mechanical and Industrial Engineering, College of Engineering, Majmaah University, Al Majmaah, 11952, Saudi Arabia; yasser.abdelrhman@mu.edu.sa (Y.A.); o.abdelaal@mu.edu.sa (O.A.)
[2] Industrial and Manufacturing Engineering Department (IME), Egypt-Japan University of Science and Technology (E-JUST), Alexandria 21934, Egypt; ibrahemmaher@eng.kfs.edu.eg
[3] Department of Mechanical Engineering, Faculty of Engineering, Kafrelsheikh University, Kafrelsheikh 33516, Egypt
[4] Mechanical Design and Production Engineering Department, Faculty of Engineering, Assiut University, Assiut 71515, Egypt
* Correspondence: saldahash@mu.edu.sa

Abstract

Understanding erosion–corrosion mechanisms in selective laser-melted (SLM) Ti-6Al-4V is essential for optimizing component durability in demanding sectors such as oil and gas, hydropower, and offshore engineering, where slurry-induced degradation prevails. Nevertheless, it is challenging to experimentally evaluate slurry erosion–corrosion over a wide range of SLM processing parameters and various slurry erosion–corrosion operating conditions. The adaptive neuro-fuzzy inference system (ANFIS) offers a robust computational approach for modeling complex systems with independent variables, making it well suited for this investigation. This study aims to assess the efficacy of ANFIS in predicting the mass loss of as-built SLM-processed Ti-6Al-4V under slurry erosion–corrosion conditions, with a focus on the synergistic effects of impact angle and erodent mass in both saline and pure water environments, validated against empirical data. The quantitative analysis reveals that erodent mass is the dominant factor influencing mass loss, followed by impact angles. Notably, the combined effect of erodent mass and impact angles in saline environments (e.g., sea water) exacerbates material loss by approximately 16% compared to pure water, highlighting the critical role of electrochemical corrosion in synergy with mechanical erosion. The results demonstrate that the ANFIS model accurately simulates the degradation behavior of SLM-processed Ti-6Al-4V subjected to water–silica slurry impacts within the experimental parameter space; however, predictive generalization beyond these conditions should be interpreted carefully due to validation constraint.

Keywords: ANFIS; Selective Laser Melting (SLM); Ti-6Al-4V; slurry erosion–corrosion

Check for updates

Academic Editor: Wenchao Zhou

Received: 22 January 2026
Revised: 28 February 2026
Accepted: 3 March 2026
Published: 6 March 2026

Copyright: © 2026 by the authors. Licensee MDPI, Basel, Switzerland. This article is an open access article distributed under the terms and conditions of the Creative Commons Attribution (CC BY) license.

1. Introduction

Metal Additive Manufacturing (MAM) represents a fundamental departure from traditional subtractive and formative production methods. Unlike conventional approaches that rely on machining tools and extensive support equipment, MAM utilizes digital 3D model data to fabricate components through the successive fusion of metallic layers, eliminating the need for tooling, fixtures, coolants, and other auxiliary manufacturing devices. There are different types of MAM technologies; each has its unique strengths

and limitations. MAM techniques are grouped into different types depending on how metallic powder is deposited, melted, or sintered. Powder Bed Fusion (PBF) is the key MAM category that primarily comprises Laser-Based PBF, such as Selective Laser Melting (SLM) and Direct Metal Laser Sintering (DMLS), as well as Electron Beam-Based PBF, which includes the Electron Beam Melting (EBM) process. These methods involve using lasers or electron beams to selectively melt or fuse very thin successive layers of metal powder on a build plate. Metal alloys such as titanium and aluminum, as well as steel and cobalt chromium alloys, are the most widely processed alloys. SLM currently has become a promising choice for producing functional metal parts in many industries because it can create intricate components with strong mechanical properties and efficiency in material use from various metallic alloys.

SLM is a Powder Bed Fusion additive manufacturing process that utilizes a high-energy laser beam to selectively melt and fuse fine metallic powder particles in a layer-wise fashion. The process occurs within an inert gas-controlled build chamber, where a recoating mechanism deposits successive powder layers onto a build platform. Through precise laser scanning of each cross-sectional layer derived from 3D CAD data, fully dense metal components are fabricated additively without requiring tooling or support for most geometries. SLM processing parameters play a critical role in determining the final quality, mechanical properties, density, surface finish, and microstructure of the printed part. Key SLM process parameters include Laser Power, Scan Speed, Layer Thickness, Hatch Spacing, Beam Diameter, Build Orientation, Inert Gas Atmosphere, and powder characteristics. SLM is highly valued for its exceptional ability to process Ti-6Al-4V alloys, known for their corrosion resistance, biocompatibility, high strength, and lightweight characteristics. While Ti-6Al-4V has long been established in Biomedical, military, and aerospace applications, it is now finding increasing use in marine, chemical processing, oil and gas extraction, and hydro-power generation applications [1–5]. The synergy between SLM's manufacturing capabilities and Ti-6Al-4V's inherent properties makes SLM-produced Ti-6Al-4V (referred to as SLMed Ti-6Al-4V) a promising option for fabricating components used in slurry and chemical handling applications. Generally, components within these applications are typically subjected to slurry erosion–corrosion—a phenomenon leading to the deterioration of materials. This occurs when solid particles suspended in a liquid medium cause both mechanical wear through particle impact and chemical corrosion from the liquid. This behavior is especially problematic in slurry-handling components, resulting in accelerated material loss, shortened component lifespan, and increased repair expenses, which can result in significant financial losses [1]. Material characteristics, solid particle properties, impact angle and velocity, slurry composition, and flow conditions are the most important factors influencing slurry erosion–corrosion. Slurry erosion–corrosion can be characterized using a variety of approaches, including weight loss measurements, surface analysis, electrochemical techniques, mechanical testing, and computational methods. However, when processed using SLM, Ti-6Al-4V undergoes rapid solidification cycles, resulting in a non-equilibrium structure that differs dramatically from the microstructures observed in traditionally processed Ti-6Al-4V (i.e., forging, casting, powder metallurgy, machining, and joining) [6]. The SLM process's high cooling rates (10^3–10^6 K/s) are primarily responsible for this difference. As a result, the Ti-6Al-4V produced through this process is expected to display distinctive properties and, consequently, a unique synergistic response to erosion–corrosion conditions. This presents significant research challenges in explaining the combined effects of SLM processing parameters and erosion–corrosion environmental factors on the degradation behavior of additively manufactured Ti-6Al-4V alloys. The complex interplay between Build Orientation, laser parameters, powder characteristics, and operational conditions (including impact angle, erodent properties, and corrosive media) necessitates a compre-

hensive investigation to establish predictive models for material performance. Therefore, for slurry-handling industrial applications to take full advantage of AM, understanding the mechanisms of erosion and corrosion and their synergistic effects is critical for developing SLMed Ti-6Al-4V that can withstand such conditions. For SLMed Ti-6Al-4V, independent corrosion studies have emerged recently [7–13]. These studies demonstrated that the SLM process produces a unique microstructure and surface condition that affects the alloy's electrochemical behavior, and SLMed Ti 6Al 4V does not have a single corrosion rating. They also demonstrated that SLMed Ti-6Al-4V exhibits good corrosion resistance, as long as process parameters, surface finishing and treatment techniques are properly set. However, dedicated slurry erosion studies have not been carried out yet [14], and even synergistic slurry erosion–corrosion studies are scarce [15]. Thus, there is a significant gap in studies of the slurry erosion–corrosion properties of SLMed Ti-6Al-4V. Nonetheless, it is noteworthy that there is a concurrent need for thorough bulk erosion–corrosion studies of SLMed Ti-6Al-4V itself, even when considering integrated surface engineering approaches such as the Magnetic Field-Assisted Laser Cladding method reported by Qi et al. [16], in order to lay the foundation for effective slurry erosion–corrosion protection strategies. These research gaps are acute for SLM Ti-6Al-4V due to two factors. The first factor is the fact that SLM is a relatively new process for producing Ti-6Al-4V compared to the conventional manufacturing methods. The second factor is the absence of standardized testing procedures. Such factors have limited the current understanding of how SLMed Ti-6Al-4V performs under slurry erosion–corrosion conditions, even though the Ti-6Al-4V finds a wide application spectrum in slurry-handling environments.

Recently, however, there has been an increasing focus on soft computing modeling techniques for the prediction of the tribological characteristics of parts produced by AM, anticipated to help address the aforementioned gap [17–29]. This is motivated by the multiple AM process parameters, target material properties, and diverse testing conditions, as well as considerations of material and manufacturing costs and the demands of extensive experimental work. One such approach is the adaptive neuro-fuzzy inference system (ANFIS), which combines the learning capabilities of artificial neural networks with the reasoning abilities of fuzzy logic. This makes it a powerful tool for analyzing and predicting the performance of systems with uncertainties and imprecisions [23,29,30]. It helps in minimizing process variability and cutting down on experimental cost while also saving time and offering a clear performance assessment. Recent studies have successfully applied ANFIS to predict tribological characteristics, including erosion–corrosion and surface roughness, in fused deposition modeling processed polylactic acid [20,27,31]. However, the application of ANFIS for modeling slurry erosion–corrosion in Selective Laser Melting (SLM) produced Ti-6Al-4V remains in its early stages. This presents an opportunity for further research and development in applying ANFIS to understand and predict the behavior of SLM-manufactured Ti-6Al-4V under slurry erosion–corrosion conditions.

The primary contribution of this research lies in the convergence of three distinct elements: the investigation of a modern, additively manufactured material, the application of advanced computational modeling for a specific optimization goal, and the rigorous validation of this model against conventional statistical benchmarks. While the erosion behavior of wrought Ti-6Al-4V is documented, its performance when produced via Selective Laser Melting (SLM) remains critically underexplored. This research provides the first systematic investigation into the synergistic effects of slurry impact angle and erodent mass on the mass loss of SLM-manufactured Ti-6Al-4V. Moreover, the novelty is not the use of ANFIS itself, but its strategic application to achieve a tangible engineering outcome. The model is employed to not only predict mass loss but, more importantly, to optimize the manufacturing and operational parameters (specifically medium type, impact angle,

and erodent mass) to minimize material degradation. This transforms the work from a descriptive case study into a prescriptive tool, offering specific, data-driven recommendations for improving the durability of SLM-produced components. Additionally, to address the use of a smaller dataset and justify the neuro-fuzzy approach, the ANFIS model is not presented in isolation. Its performance is rigorously benchmarked against simpler, well-established statistical techniques, including Linear Regression, and validated using Analysis of Variance (ANOVA). This comparative framework quantitatively demonstrates that ANFIS captures complex, non-linear interactions between variables (interactions that simpler models fail to identify), leading to a superior predictive accuracy and providing a clear mathematical justification for its application.

2. Materials and Methods

In this study, experimental data of the mass loss of as-built Ti-6Al-4V samples were collected from the previously published literature [32] to develop and compare the corresponding ANFIS model. The manufactured specimens at similar building conditions were tested under different slurry impact conditions (impact angle and mass of erodent) in two different mediums (tap water and saline water). An overview of the experimental work is described below.

2.1. Materials and Manufacturing

Spherical Ti-6Al-4V powder supplied by Renishaw plc (Stone, Staffordshire, UK (chemical composition: Table 1; morphology: Figure 1) had a manufacturer-specified mean particle size of ~30 µm, validated by an independent particle size distribution analysis of an identical powder (mean = 31.42 ± 9.27 µm) by Peng et al. [33]. Under Ar gas protection with parameters in Table 2, the SLM-AM250 system (Renishaw, Staffordshire, UK) produced 23 × 10 × 2.5 mm specimens mounted on the build platform, as shown in Figure 2. The system is equipped with an ytterbium (Yb) fiber laser delivering a wavelength of 950 nm. Following manufacturing, a standard metallographic procedure was used to prepare their surfaces for slurry erosion–corrosion testing. Grinding was carried out using SiC sheets with grit sizes of 240, 600, 1200 and 2500, followed by mirror polishing using a polishing cloth with diamond particles of sizes 6, 3 and 1 µm. The samples then underwent a final cleaning step using distilled water. To reveal the microstructure, polished specimens were chemically etched for 5–10 s using a 10% HF, 5% HNO_3, and 85% distilled water solution. Post-etching, specimens underwent ultrasonic degreasing in C_2H_5OH for 600 s, followed by forced convection drying via heated compressed air.

Table 1. Chemical composition (weight percentage) of the SLM-processed Ti-6Al-4V alloy.

Element	Ti	Al	V	C	Fe	O	N	H	Yttrium
wt. %	Balance	5.50–6.50	3.50–4.50	≤0.08	≤0.25	≤0.13	≤0.05	≤0.012	≤0.005

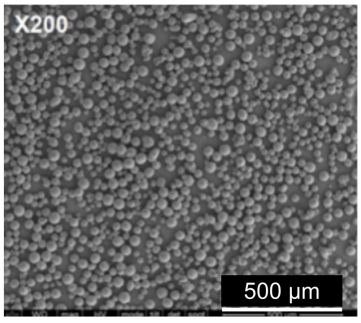

Figure 1. SEM image of Ti-6Al-4V powder morphology.

Table 2. Process parameters for selective laser melting (SLM) of Ti-6Al-4V.

Laser Power (W)	Laser Spot Size (μm)	Scanning Speed (mm/s)	Layer Thickness (μm)	Hatch Spacing (mm)	Exposure Time (μs)	Hatching Strategy	Atmosphere
200	75	857	60	0.095	140	Meander	Argon gas

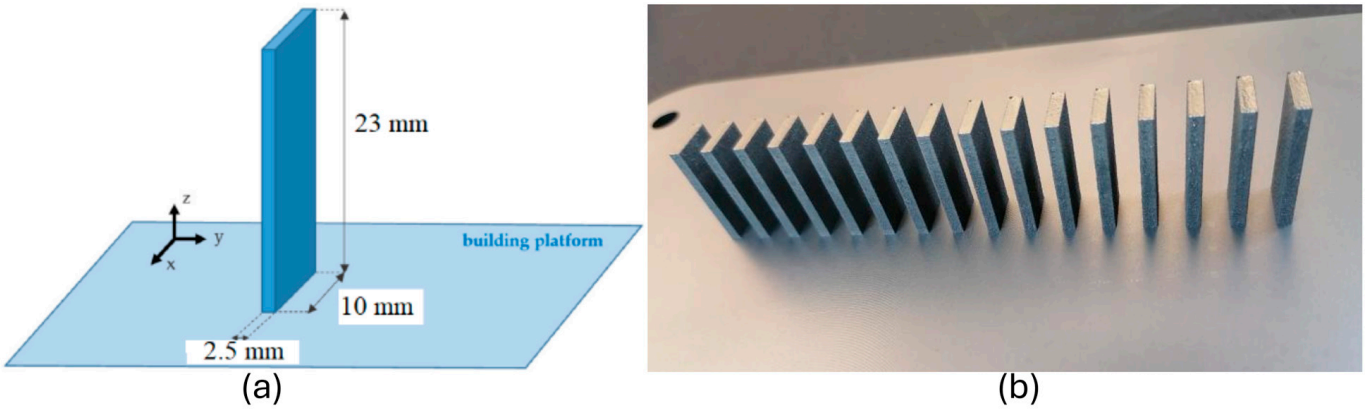

Figure 2. (**a**) Dimensions of slurry erosion–corrosion specimen. (**b**) Photo of the batch oriented on the build platform.

2.2. Slurry Erosion–Corrosion Experimental Setup

The experimental setup consisted of the same elements as previously described in [32]. Briefly, the slurry erosion–corrosion behavior of as-built SLM Ti-6Al-4V was evaluated using a whirling arm test apparatus (Figure 3). Initial experiments employed tap water–sand slurry exclusively. Prior to testing, two identical polished SLMed specimens were ultrasonically cleaned, oven-dried, and precision-weighed before mounting on adjustable-angle holders at the ends of the whirling arms. The specimens were positioned at predetermined impact angles within the slurry chamber. Second, a uniform slurry in a 25-L tank was transferred via a pipe to the slurry test chamber and fed into a funnel that had a stirrer to maintain the suspension of the slurry. The funnel was then directed to a 3 mm diameter orifice that was 40 mm from the specimen surface. The slurry flowed out of the orifice under gravity and impacted on the center of the whirling specimen surfaces. The falling velocity of the slurry was $v_1 = 1.67\,\mathrm{m/s}$, producing continuous impacts on the specimen surface. The main contribution to the impact velocity resulted from the rotational motion of the whirling arms, with a linear velocity of $v_2 = 14.96\,\mathrm{m/s}$. Accordingly, the resultant impact velocity was approximately 15 m/s. For more details regarding the experimental procedure and the test rig configuration to ensure reproducibility, see ref. [34]. Experiments were done at room temperature at four different impact angles (30°, 45°, 60°, and 90°), with five measurement intervals for each angle. Finally, the specimens were removed from the test chamber and ultrasonically cleaned in acetone both before and after each test session. Following preparation, specimens were dried and weighed using a precision balance (±0.1 mg accuracy). For each test condition, two specimens were measured with five replicates per specimen, with the arithmetic mean mass loss calculated per impact angle. In subsequent experiments, the same methodology was employed using a modified slurry containing: 10 g/L (1 wt.%) SiO_2 particles and 3.5 wt.% NaCl electrolyte solution.

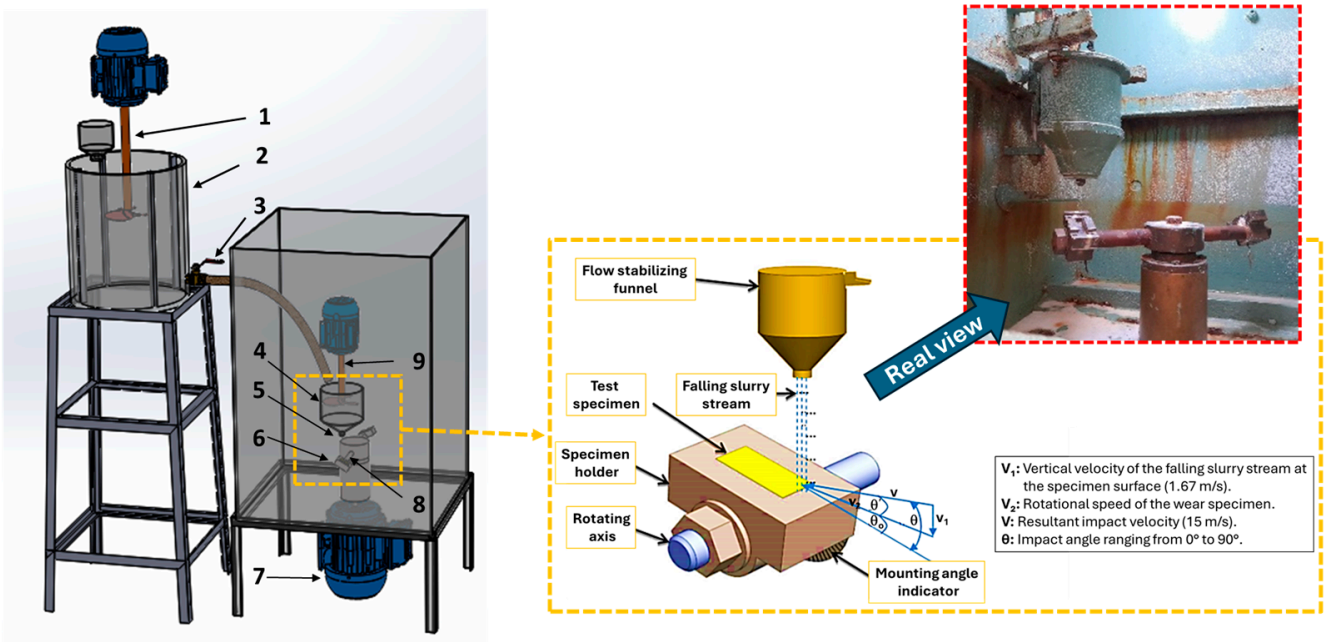

Figure 3. The whirling arm slurry erosion test apparatus.

2.3. Energy Dispersive X-Ray Spectroscopy (EDX) and Microstructure

The FEI Quanta FEG 450-SEM (FEI Co., Hillsboro, OR, USA) is used to characterize and determine a sample's elemental composition through X-ray detection using a silicon drift detector (SDD) EDS detector, operated at 20 kV. The FEI Quanta 450 FEG SEM was also used to examine the microstructure of the etched sample and the surface morphology of the unpolished SLM-produced specimens. A JEOL JSM 5400 scanning electron microscope (JEOL Ltd., Tokyo, Japan) was employed to characterize the surface microstructure of the eroded samples.

2.4. Data Analysis Methodology

A dual-methodology approach was adopted to analyze the data, consisting of statistical analysis to identify significant factors (ANOVA) and predictive modeling to map the complex process behavior (ANFIS modeling). This experiment investigated the effects of media type (pure water vs. sea water), impact angle (IA) at four levels, 30, 45, 60, and 90 degrees, and mass of erodent (MP) at five levels, 28.2, 56.4, 84.6, 112.8, and 141.0 g, on the response variable mass loss (ML). The study employed a full factorial design with 40 observations (2 media × 4 IA levels × 5 MP levels), providing a robust dataset for examining both main effects and interactions.

2.4.1. Statistical Analysis

The collected data was first analyzed using regression and ANOVA in Minitab 16 software to determine the statistical significance of the factors and their interactions. All statistical tests were conducted at a 95% confidence level. The regression metrics obtained are R^2 = 0.9554, adjusted R^2 = 0.9517, RMSE = 0.0913, MAE = 0.074, and MAPE = 28.47%. Additionally, Table 3 shows the ANOVA effect size (three-way) metrics.

Table 3. Three-way ANOVA metrics.

Effect	F-Value	*p*-Value	η^2	Partial η^2	Interpretation
Media	171.62	<0.001	0.127	0.867	Large effect
IA	128.43	<0.001	0.286	0.928	Very large effect
MP	585.24	<0.001	0.434	0.983	Extremely large effect
Media × IA	3.89	0.022	0.009	0.304	Small effect
Media × MP	16.19	<0.001	0.012	0.653	Medium effect
IA × MP	8.83	<0.001	0.039	0.780	Large effect
Media × IA × MP	2.06	0.076	0.009	0.439	Not significant (p = 0.076)

2.4.2. ANFIS Model

Every smart strategy has unique computational characteristics that make it suitable for specific problems. For example, neural networks excel at pattern recognition, but they are inadequate in explaining their decision-making processes. On the other hand, fuzzy logic frameworks, which can accommodate uncertain records, are proficient in explaining their choices but are incapable of robotically acquiring the rules they utilize to manage such decisions. These restrictions have been a key motivator for the development of smart mixed approaches, which combine two or more methodologies to overcome the drawbacks of individual approaches.

To enable a system to manage mental doubt in a manner more akin to humans, fuzzy logic can be combined with neural networks. The computational process of ANFIS begins with developing an ANFIS model inspired by biological neuronal structures, followed by training mechanisms. There are three stages in ANFIS modeling:

1. Development of an ANFIS based on biological neurons,
2. Creating a synaptic connection structure that integrates fuzziness into the neural network,
3. Development of learning algorithms.

To enhance decision-making processes, neural networks fine-tune the membership functions within fuzzy logic systems. While fuzzy logic can directly capture expert knowledge through rules with linguistic labels, designing and adjusting these membership functions often demands considerable effort. The integration of neural network training systems automates this process, yielding faster development, reduced costs, and superior performance [35].

The ANFIS architecture, illustrated in Figure 4, combines neural network processing with fuzzy logic. The system develops input–output relationships through two knowledge sources: human-derived fuzzy rules and pre-collected training data for neural network adaptation. The ANFIS model calculates the membership function parameters to align with the known experimental input–output data.

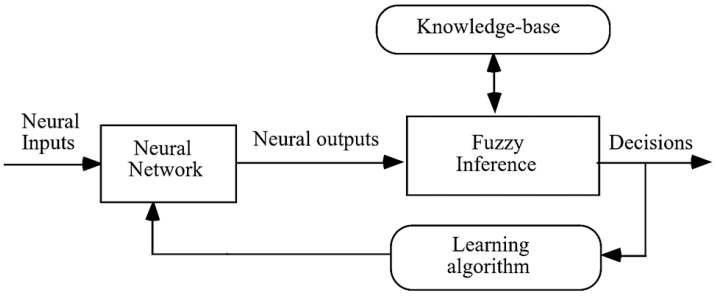

Figure 4. Fuzzy neural system model [35].

The ANFIS model was implemented through the utilization of MATLAB R2014a software. The training of ANFIS employed various membership functions, with four triangle membership functions being chosen for impact angle and five for mass erodent, as shown in Figure 5. The creation of the neuro-fuzzy model involved the selection of triangular membership functions, which resulted in the lowest training error for mass loss. The training phase comprised 50 learning cycles using the output values, yielding an average error of 5.96×10^{-7} (Figure 6). Due to its high precision, this method was selected for ANFIS optimization. The system's fuzzy rules, implemented with triangular membership functions, followed the Sugeno inference scheme (Figure 7).

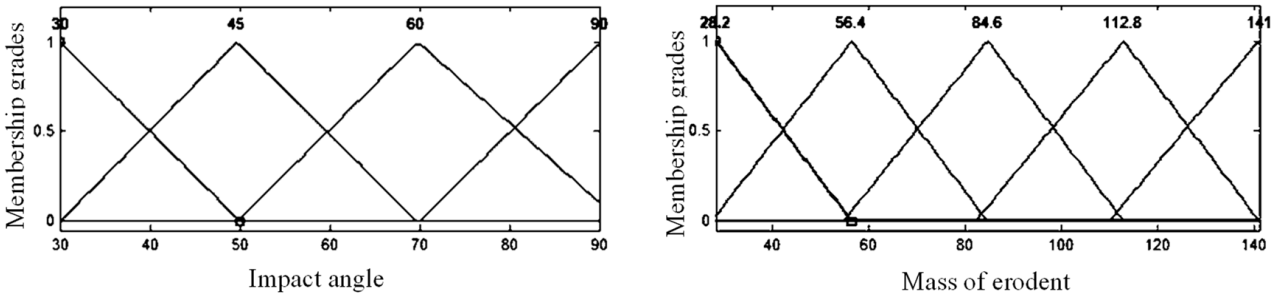

(**a**) (**b**)

Figure 5. Post-training membership functions of input parameters: (**a**) membership functions of impact angles; (**b**) membership functions of mass of erodent.

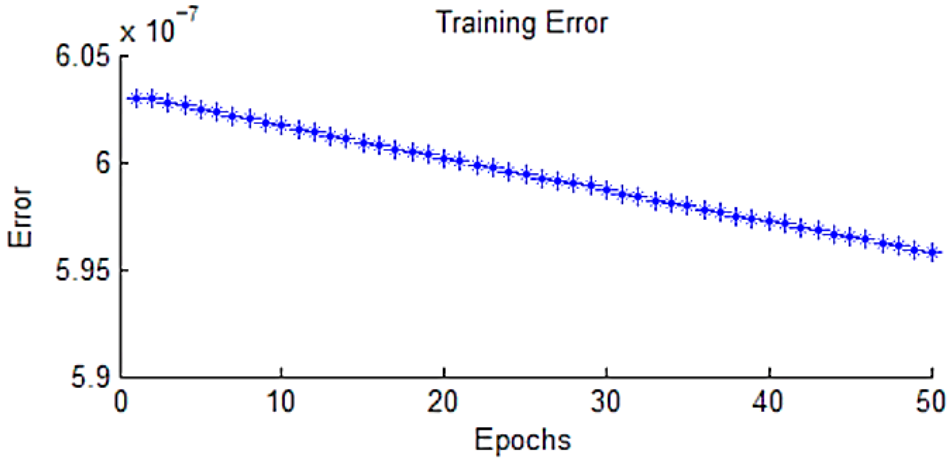

Figure 6. Training error of the triangular membership function.

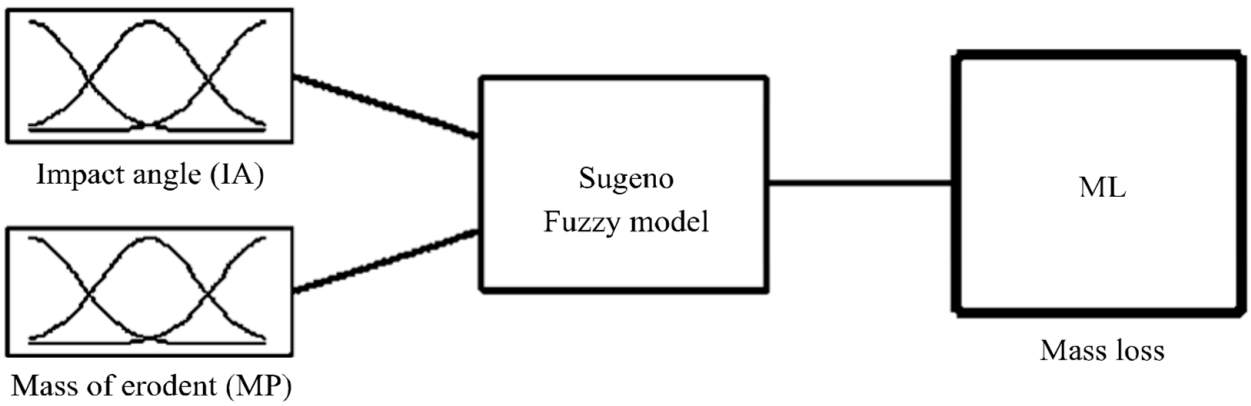

Figure 7. Fuzzy role construction of the triangular membership function.

The ANFIS utilizes a series of five network levels to execute the fuzzy analysis process, as depicted in Figure 8. These layers consist of input parameters in layer one, a fuzzy set database layer in layer two (input membership function), a fuzzy rule base structure layer in layer three, a decision-making layer four (output membership function), and an output defuzzification layer in layer five. Further details regarding this process can be found in the literature [36,37].

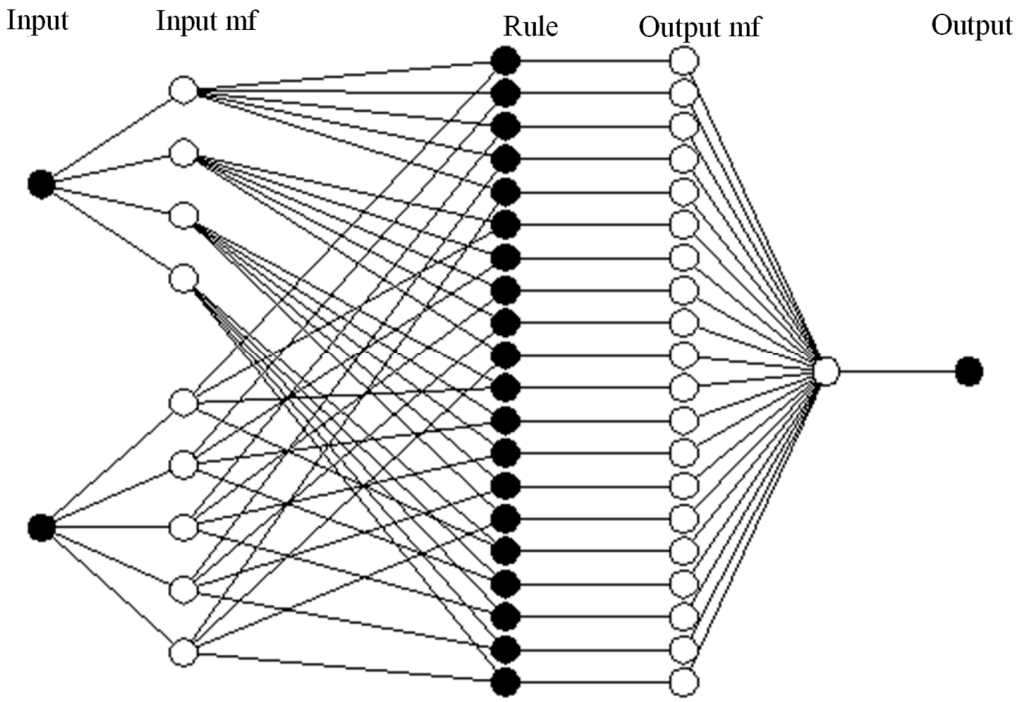

Figure 8. ANFIS construction for Sugeno technique.

The subsequent discussion shall expound upon the five distinct levels:

Level 1: Fuzzification: Each node's output reflects the input's compatibility with its linguistic label. Triangular membership functions are adopted here due to their efficacy in representing linear input–output mappings for verbal terms.

First parameter membership functions

$$A_i(IA) = \begin{cases} 1 - \frac{|a_i - IA|}{\alpha_i} \; if \; |a_i - IA| \leq \; \alpha_i \\ 0 \qquad\qquad\qquad\qquad Otherwise \end{cases} \tag{1}$$

Second parameter membership functions

$$B_i(MP) = \begin{cases} 1 - \frac{|b_i - MP|}{\beta_i} \; if \; |b_i - MP| \leq \; \beta_i \\ 0 \qquad\qquad\qquad\qquad Otherwise \end{cases} \tag{2}$$

where $\{a_i, \alpha_i, b_i,$ and $\beta_i\}$ are the parameter set.

As these parameters vary, the shapes of the corresponding membership functions adapt dynamically, as demonstrated in Figure 5. This visualization captures the diverse forms of membership functions for linguistic labels A_i and B_i. The parameters at this level are designated as premise parameters.

Level 2: Rule Evaluation: Each node in this layer calculates the firing strength of its corresponding fuzzy rule. These nodes are specifically designated as rule nodes, representing the application of the fuzzy AND operator (typically implemented as multiplication or minimum operation) to the incoming membership degrees.

The top neuron's output

$$w_1 = A1(IA) \times B1(MP) \tag{3}$$

The bottom neuron's output

$$w_n = A4(IA) \times B5(MP) \tag{4}$$

Level 3: Normalization: Each node in this layer, denoted by N, normalizes the firing strengths by computing the ratio of each rule's firing strength to the sum of all rules' firing strengths.

The top neuron's output

$$\overline{w}_1 = \frac{w_1}{w_1 + w_2 + \ldots + w_n} \tag{5}$$

The bottom neuron's output

$$\overline{w}_n = \frac{w_n}{w_1 + w_2 + \ldots + w_n} \tag{6}$$

Level 4: Rule Output Processing: Each node in this layer computes the weighted rule consequence by multiplying the normalized firing strength (from Level 3) with the corresponding rule output function (typically a linear combination of inputs for first-order Sugeno systems).

The top neuron's output

$$\overline{w}_1 F1 \; = \; \overline{w}_1 \; (a1IA \; + \; b1MP) \tag{7}$$

The bottom neuron's output

$$\overline{w}_n Fn \; = \; \overline{w}_n (anIA \; + \; bnMP) \tag{8}$$

Level 5: Output Aggregation: The single node in this final layer computes the system's overall output through the summation of all incoming weighted rule consequences from Level 4, effectively performing defuzzification in Sugeno-type ANFIS architectures.

$$ML \; = \; \overline{w}_1 F1 \; + \; \overline{w}_2 F2 \; + \; \ldots \; + \; \overline{w}_n Fn \tag{9}$$

Given a crisp training dataset $\{(x_k, y_k), k = 1, \ldots, K\}$, the ANFIS model parameters can be optimized through gradient-based learning methods. The error function for each training pattern k is defined by the squared output difference, as shown in the following equation:

$$Ek = (yk - ok)2 \tag{10}$$

where yK is the target output value (ground truth), and oK is the ANFIS model's predicted output.

3. Results and Discussion

3.1. Energy-Dispersive X-Ray (EDX) Spectroscopy Analysis

The EDX analysis after the SLM processing of Ti-6Al-4V confirms a Ti-rich alloy (Figure 9) containing Al (5.30 wt.%) and V (2.78 wt.%). Table 4 presents chemical EDX mass fractions (wt%) obtained from multiple scan areas on SLMed Ti-6Al-4V compared to the manufacturer's nominal composition. While the measured Al content is close to

the nominal Ti-6Al-4V specification, the V content appears lower than the nominal range (3.5–4.5 wt.%). The variation is most likely the result of the localized dispersion of alloying elements caused by SLM's inherent fast cooling and solidification. Cooling rates can cause micro-structural changes, including the increased formation of α′ martensite in regions with reduced β-stabilizer (vanadium) content, resulting in localized regions with slightly different concentrations of alloying elements [12,38,39], in addition to the surface-sensitive nature of EDX measurements.

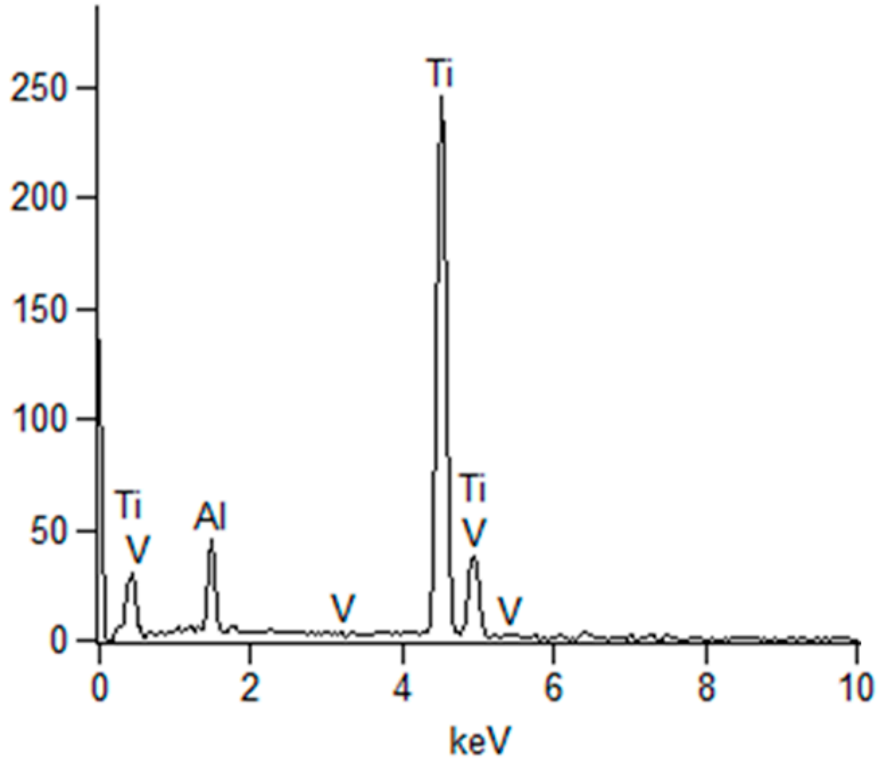

Figure 9. (EDX) spectroscopy analysis of SLM-processed Ti-6Al-4V.

Table 4. Quantitative EDX mass fractions (wt%) from multiple scan areas on SLMed Ti-6Al-4V compared to the manufacturer's nominal composition.

Element	EDX Measured (wt.%)	Nominal Composition (wt.%)	Comparison
Al	5.30 ± 0.31	5.50–6.50	Close (slightly low)
V	2.78 ± 0.75	3.50–4.50	Lower than nominal
Ti	91.92 ± 1.74	Balance (~88–89 nominal)	Consistent
Minor elements	Not detected	Present in trace amounts	Below EDX detection

3.2. External Surface Morphology

Defect formation is a common challenge in SLM. As shown in Figure 10, the outside surface of unpolished as-built Ti-6Al-4V samples displays visible characteristics such as unmelted powder and partly melted powders adhering to the surface, as well as surface cracks and lack-of-fusion gaps that reveal distinct paths. While cutting-edge SLM systems and optimized building conditions may significantly reduce defect rates, producing a completely defect-free as-built SLM-produced Ti-6Al-4V surface remains difficult due to the inherent nature of the layer-by-layer melting and cooling process [38].

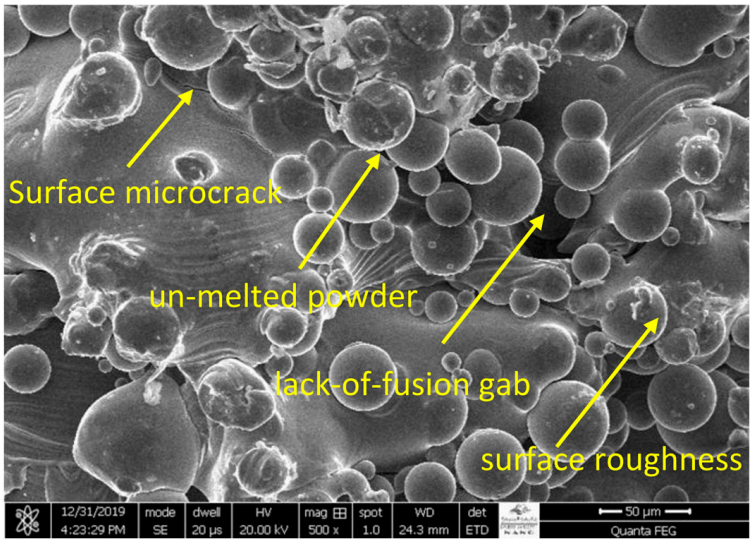

Figure 10. Scanning electron micrograph illustrating the surface topography of unpolished as-built SLM-produced Ti-6Al-4V.

3.3. As-Built SLM-Produced Ti-6Al-4V Microstructure

The microstructure of polished and etched as-built Ti-6Al-4V produced through Selective Laser Melting (SLM) is illustrated in Figure 11. Due to the rapid cooling rate during the Selective Laser Melting processing, SLMed Ti-6Al-4V typically features a fine, acicular (needle-like) α′ martensitic phase structure that emerged from the previous β particle borders. The rapid solidification results in an out-of-equilibrium microstructure that differs from the conventional (α + β) microstructures found in conventionally processed Ti-6Al-4V. Rapid cooling prevents the β phase from developing, leaving a martensitic α′ phase throughout the material. However, the α′ martensite phase shows significantly less ductility compared to traditional (α + β) phases. This reduced toughness may facilitate localized cracking and surface degradation when it is exposed to repeated slurry impacts. As a result, the net erosion–corrosion performance is predetermined by the relationship between the increased hardness and the reduced ductility. In addition, microstructural differences can influence corrosion behavior by varying passive film stability and phase distribution, which all influence the measured erosion–corrosion performance. This metastable microstructure was also commonly noted by many authors [40,41].

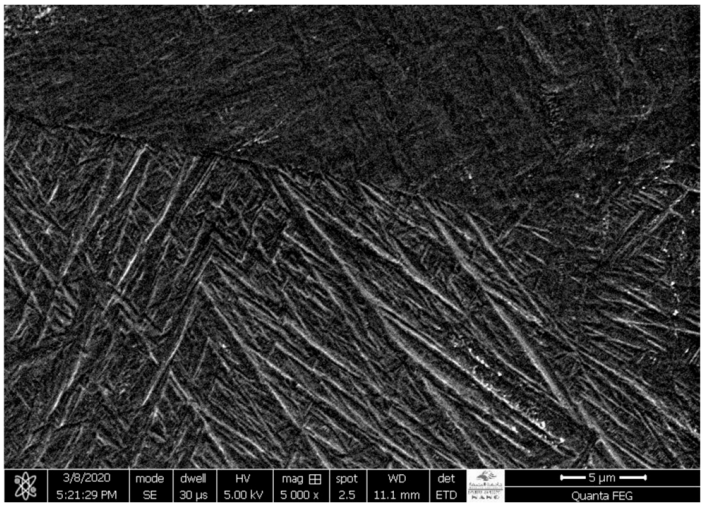

Figure 11. Microstructure of As-built SLM-produced Ti-6Al-4V.

3.4. Experimental Results of Slurry Erosion–Corrosion

Figure 12a,b show the relationship between the amount of erosion in milligrams and the angle of impact when several specified quantities of solid silica particles are loaded in a fresh tap water medium (Figure 12a) and another in a salt water (sea water) medium (Figure 12b), respectively, striking the specimens. Both figures show almost the same trend or inclination at different values of silica particles. The lowest value of erosion appears at the impact angle of 90°, while the largest value of the mass loss from the struck specimens in both studied mediums occurs at the angle of 30°, which is consistent with the known slurry erosion behavior of ductile materials [42]. As is also clear from Figure 13a,b, when increasing the number of impacting particles, which means increasing the test time, the mass loss increases linearly at all the different studied impact angles, 30°, 45°, 60°, and 90°, and in the two studied mediums, pure water and salt water, respectively. These results are attributable to the prevailing slurry erosion mechanism (see Figure 14); at low angles, the predominant mechanism of slurry erosion is ploughing, where the particles impact the surface of the specimen and make light, deep, narrow, and long grooves with chips on both blanks. By successive impacts, new particles will impact the damaged surface, causing a removal of the old-formed chips; new craters will be formed again, and the process of formation and removal will be repeated many times, causing this big mass loss at these low impact angles, i.e., 30° and 45°. Meanwhile, at high impact angles, i.e., 60° and 90°, deep and short craters (pits) will be formed and a small amount of chips will be formed around these craters, and then, by the successive impacts, the formed chips will be removed, causing a small mass loss compared to those at low impact angles; this interpretation is consistent with that of Abdelrhman et al. [43].

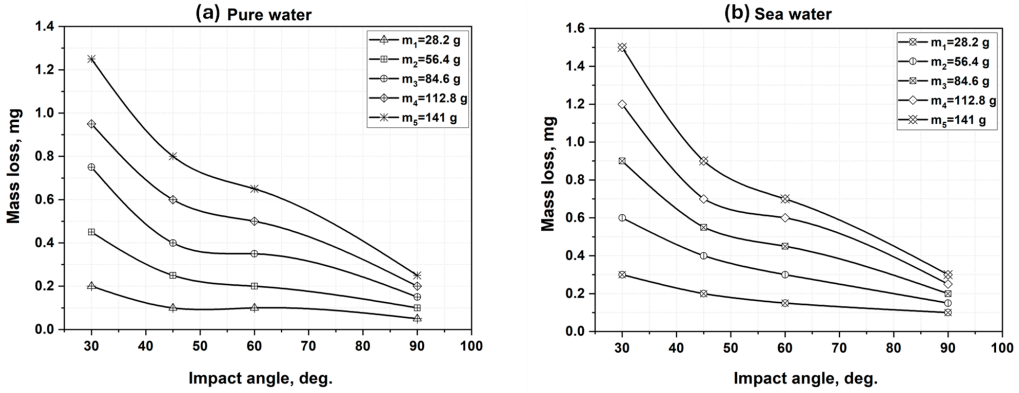

Figure 12. Mass loss as a function of impact angle at varying erodent concentrations for (**a**) pure water and (**b**) sea water.

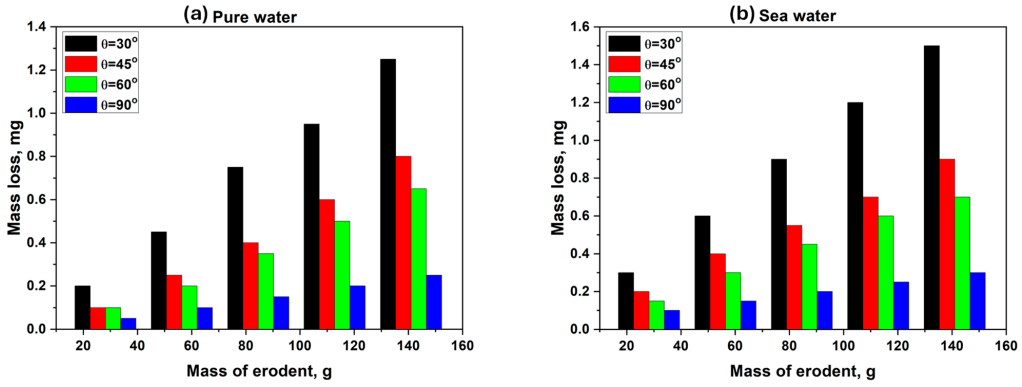

Figure 13. Mass loss as a function of erodent mass concentration at varying impact angles (30–90°) in (**a**) pure water and (**b**) sea water.

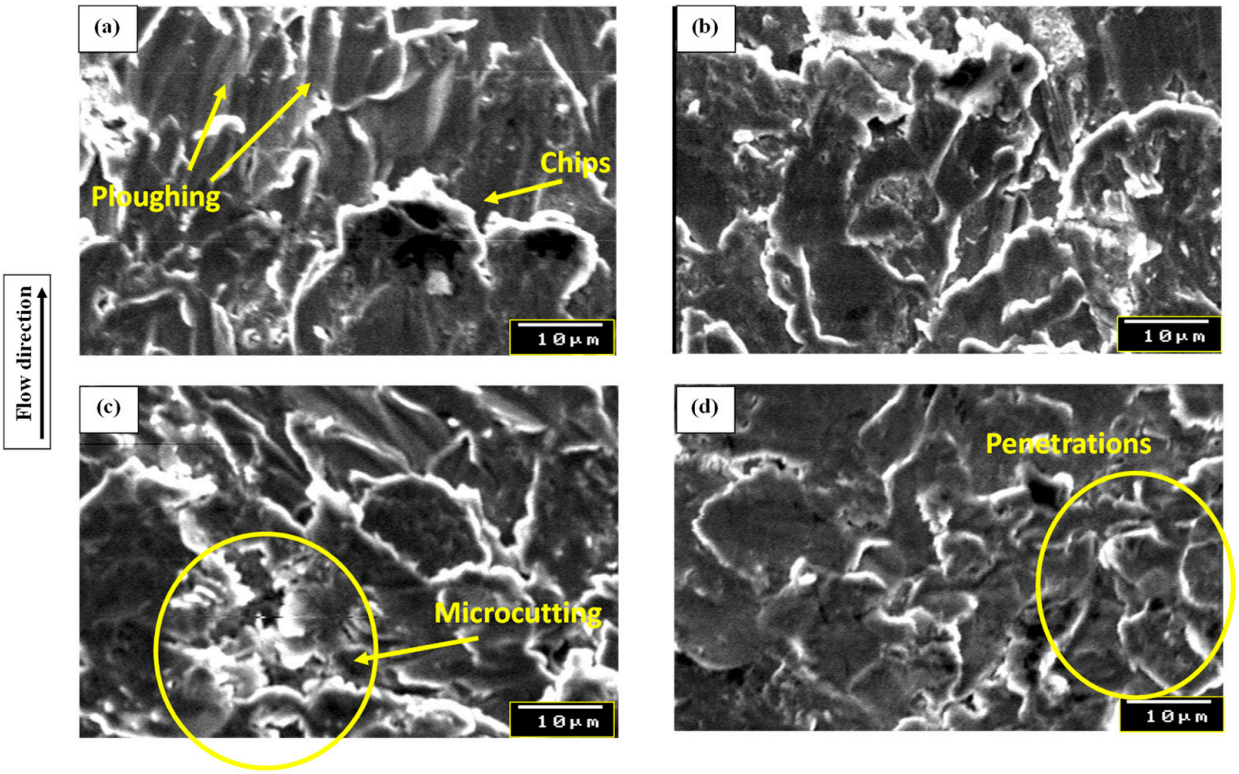

Figure 14. Surface degradation characteristics of selective laser-melted Ti-6Al-4V under slurry erosion in pure water and sea water at impact angles of: (**a**) 30°; (**b**) 45°; (**c**) 60°; and (**d**) 90°.

Figure 15 shows how mass loss varies with the aqueous medium at different impact angles. The results indicate that the cumulative mass loss of SLM-fabricated Ti-6Al-4V specimens is consistently higher in saline medium than in pure water for all investigated impact angles (30–90°).

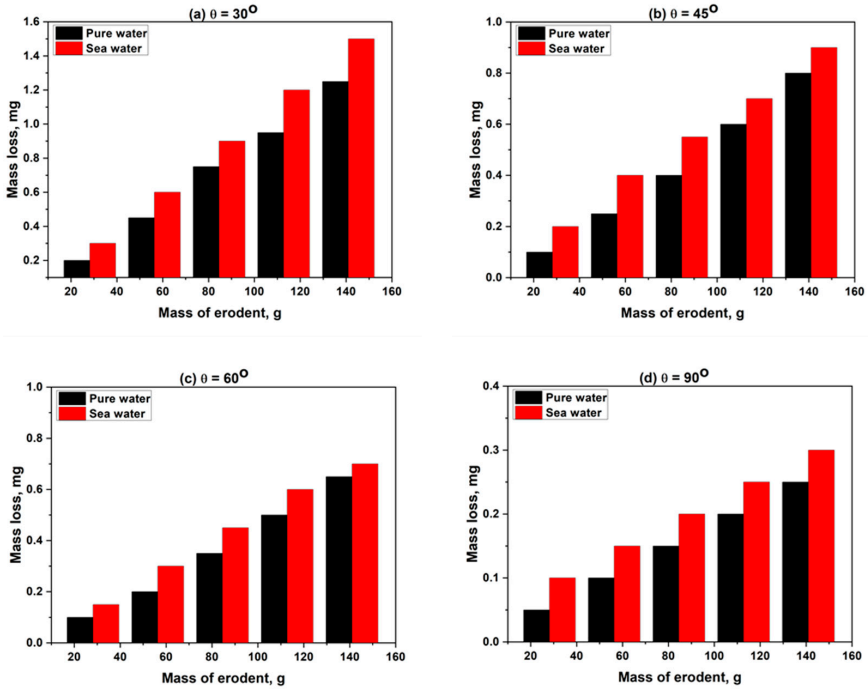

Figure 15. Comparative analysis of mass loss trends between pure water and sea water across all impact angles (30°, 45°, 60°, 90°) with increasing mass of erodent.

The observed increase in mass loss in the saline medium can reasonably be associated with the combined influence of mechanical slurry erosion and possible corrosion-related effects. Titanium alloys are known to form a chemically stable TiO_2 passive film in aqueous environments. Under repeated slurry impacts, this protective layer may be disrupted continuously. In addition, the presence of chloride ions in saline water could contribute to surface degradation. However, this interpretation remains qualitative within the scope of the present work. Electrochemical analysis is indeed possible. Nevertheless, such measurements are usually conducted under static conditions and may not accurately reproduce the highly dynamic slurry environment used in this study. For this reason, the results are presented cautiously as a higher mass loss in saline solution, rather than as a direct confirmation of specific corrosion mechanisms. These findings are consistent with previous studies reporting increased material degradation in saline slurry conditions [44,45].

Besides the general slurry erosion mechanisms discussed earlier, the acicular α' martensitic structure formed in the as-built SLM Ti-6Al-4V should also be considered when interpreting the erosion response. The fine needle-like morphology of the α' phase is typically associated with a higher hardness compared to the conventional $\alpha + \beta$ microstructure. This increase in hardness can reduce particle penetration and limit severe plastic deformation during micro-cutting. In other words, the surface becomes less susceptible to deep ploughing under impact.

At the same time, however, the α' martensitic structure is known to exhibit a lower ductility than the equilibrium $\alpha + \beta$ structure. Under repeated slurry impacts, this reduced ductility may favor localized cracking or micro-fracture at the surface. Therefore, the overall erosion behavior of the SLMed material is not governed by hardness alone. It results from the combined effect of increased hardness and reduced toughness and how these two factors interact under dynamic particle impact conditions, in comparison with conventional $\alpha + \beta$ Ti-6Al-4V.

3.5. Statistical Analysis Results and Discussion

The regression model demonstrated an exceptional predictive capability with an R^2 of 0.9554, indicating that 95.54% of the variance in ML is explained by the three factors and their interactions. The adjusted R^2 of 0.9517 confirms that this high explanatory power is not merely due to overfitting, as the penalty for multiple predictors only marginally reduces the value. This suggests that the selected factors (media, IA, and MP) are highly relevant determinants of ML.

The Root Mean Square Error (RMSE) of 0.0913 indicates that, on average, the model's predictions deviate from observed values by approximately 0.09 units. Given that ML values range from 0.05 to 1.50, this represents a relative error of about 6–10% for mid-range values. The Mean Absolute Error (MAE) of 0.074 provides a more robust measure of average prediction error, confirming the model's precision. For practical purposes, the absolute error metrics (RMSE and MAE) provide a more meaningful assessment of model performance.

3.5.1. Main Effects Analysis

Figure 16 shows the main effects of the media, IA, and MP on the means of ML.

The highly significant main effect of media ($F = 171.62$, $p < 0.001$) demonstrates that sea water consistently produces higher ML values than pure water. The regression coefficient of 0.157 indicates that, holding other factors constant, switching from pure water to sea water increases ML by an average of 0.157 mg. This represents a substantial effect, particularly considering that the overall mean ML is approximately 0.5 mg.

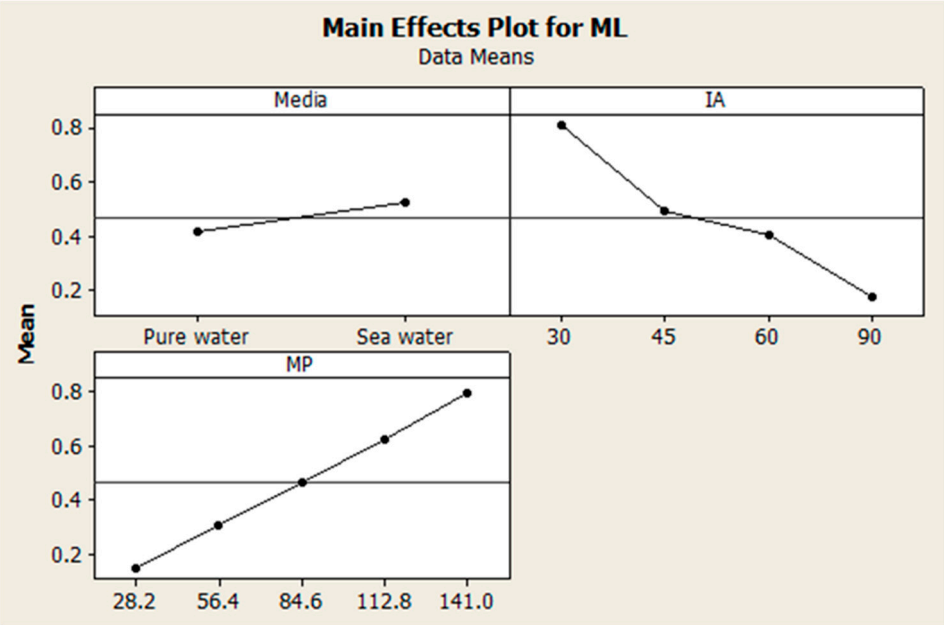

Figure 16. Main effect plots of the mean ML in relation to media, IA, and MP.

The impact angle shows a strong negative relationship with ML (coefficient = −0.0051, F = 128.43, $p < 0.001$). As IA increases from 30° to 90°, ML decreases systematically across all conditions. The effect size ($\eta^2 = 0.286$) indicates that IA explains 28.6% of the total variance in ML, making it the second most important factor after MP.

The mass of erodent exerts the strongest influence on ML (F = 585.24, $p < 0.001$, $\eta^2 = 0.434$), explaining 43.4% of all variance in the response variable. The positive coefficient (0.0081) indicates a direct relationship: as MP increases, ML increases. This is the dominant factor in the system, with nearly twice the explanatory power of IA.

3.5.2. Interaction Effects

Figure 17 shows the interaction plots of the media, IA, and MP on the ML.

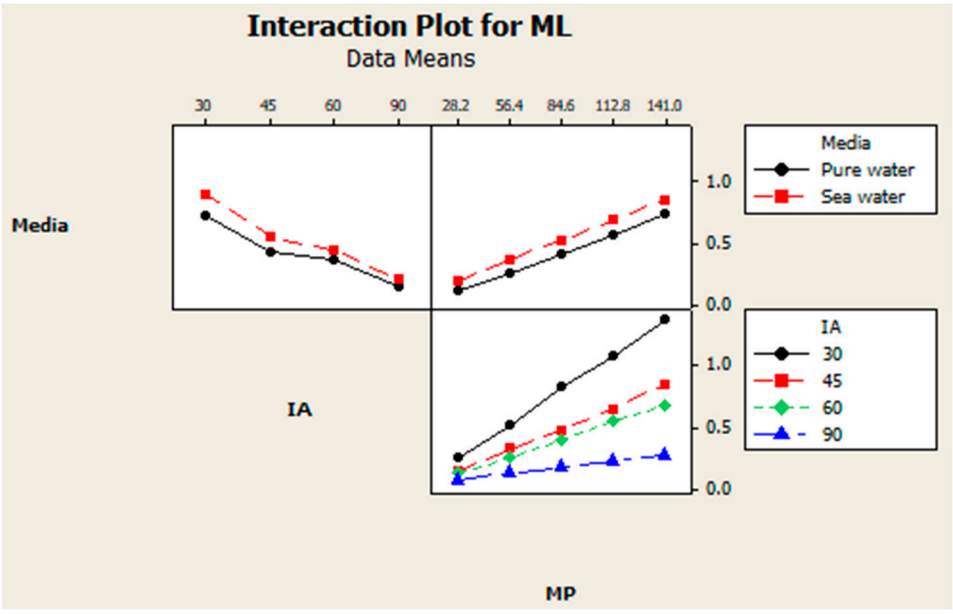

Figure 17. Interaction plots of the mean ML in relation to media, IA, and MP.

The significant media × IA interaction (F = 3.89, p = 0.022, η^2 = 0.009) indicates that the effect of IA differs between media types. While both media show decreasing ML with increasing IA, the rate of decrease is steeper in pure water than in sea water (Figure 17). This explains why the difference between media becomes more pronounced at lower IA values. The highly significant media × MP interaction (F = 16.19, $p < 0.001$, η^2 = 0.012) reveals that the concentration effect is stronger in sea water than in pure water. The IA × MP interaction is highly significant (F = 8.83, $p < 0.001$) with a large effect size (η^2 = 0.039). This indicates that the effect of concentration depends on IA, and vice versa. The three-way interaction approaches but does not achieve conventional significance (F = 2.06, p = 0.076, η^2 = 0.009). The p-value of 0.076 suggests a trend toward significance that might become significant with a larger sample size. The partial η^2 of 0.439 indicates a moderate effect size when controlling for other factors, suggesting that the complex interdependence among all three factors warrants consideration in practical applications.

3.6. ANFIS Model Analysis

In this research, a set of 20 rules was constructed for mass loss based on a full factorial design of experiments in two different mediums (tap water and saline water), as shown in Figure 18. Figures 18a and 18b depict the ANFIS model rule structure for the mass loss in relation to the impact angles and mass of erodent in pure and saline water, respectively.

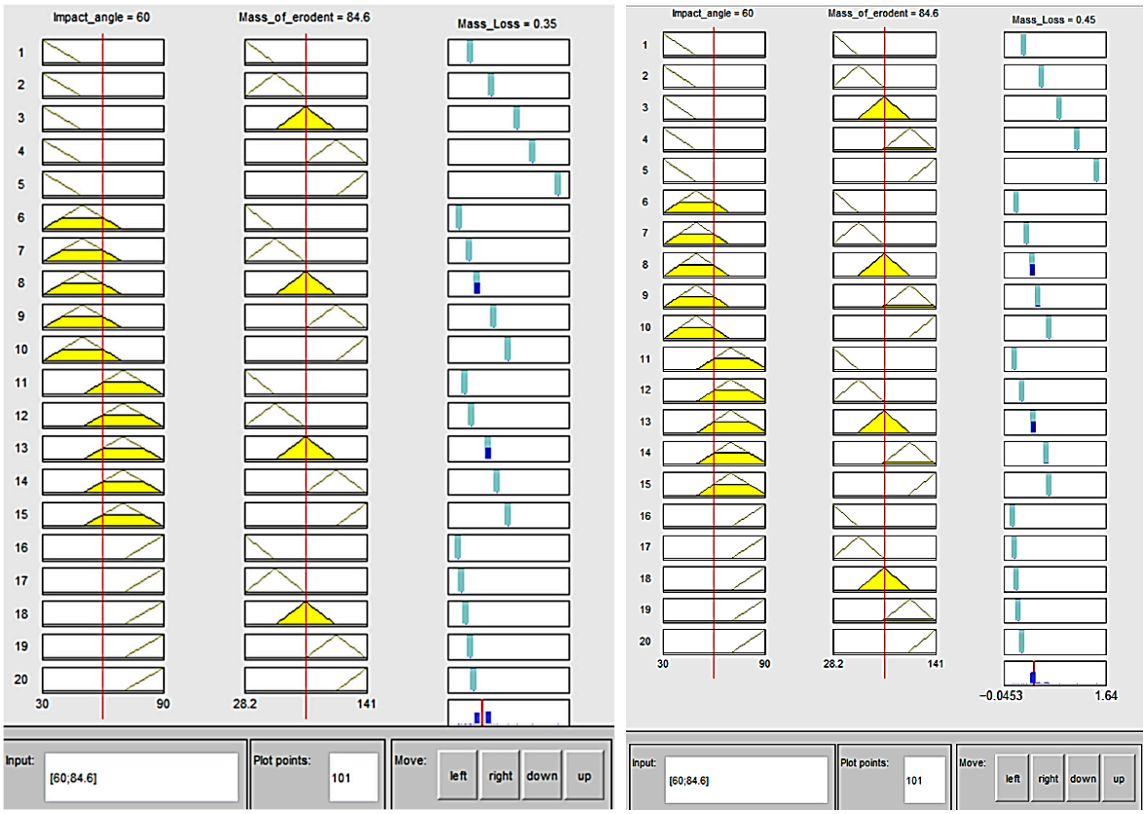

(**a**) (**b**)

Figure 18. ANFIS model rule structure for the mass loss in relation to impact angles and mass of erodent in (**a**) pure water medium; (**b**) saline water medium.

Employing the established ANFIS model, the mass loss parameters associated with Ti-6Al-4V alloy produced via SLM were derived from the two designated input variables. The ANFIS predictions showed excellent agreement with experimental measurements (R^2 = 0.9554), confirming the model's generalization capability despite the limited training data. Moreover, a post hoc power analysis confirmed that, with α = 0.05, expected effect

size $f^2 > 0.35$, and 2 predictors, the sample size of n = 40 provides a statistical power exceeding 85%.

The synergistic influence of these dual parameters on the output fluctuation of slurry erosion is illustrated in Figures 19 and 20. Specifically, Figures 19 and 20 present the surface charts that elucidate the influence of the pure and saline water parameters on the overall mass loss. According to Figures 19 and 20, the mass of the erodent (MP) has a remarkable effect subsequently to the impact angle (IA) on the total mass loss. Specifically, at low levels of impact angles, the mass of the erodent has a great impact on the mass loss. Similar observations have been found through the experimental results discussed above. The total mass loss increases with the increasing mass of erodent during all ranges of impact angles. But the mass loss increases with decreasing impact angles. Furthermore, the influence of the erodent mass and the impact angles is considerably more pronounced in saline environments (16%) compared to that of pure water.

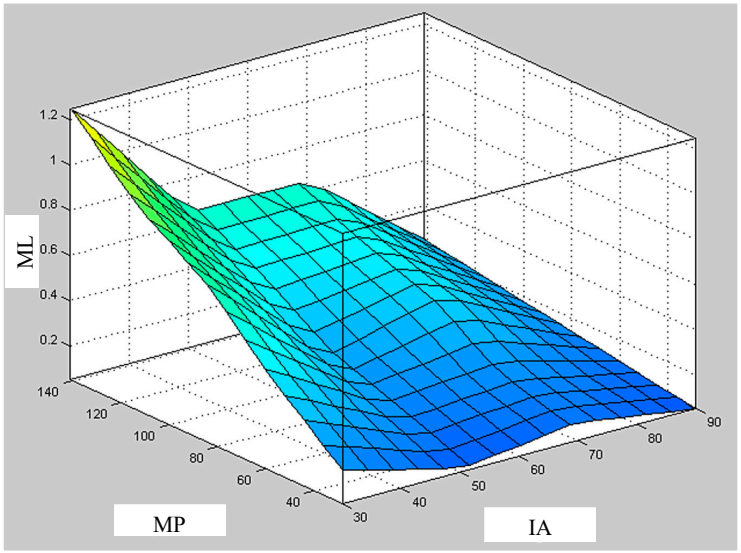

Figure 19. Mass loss (ML) in relation to change in slurry impact angle (IA) and mass of erodent (MP) using pure water.

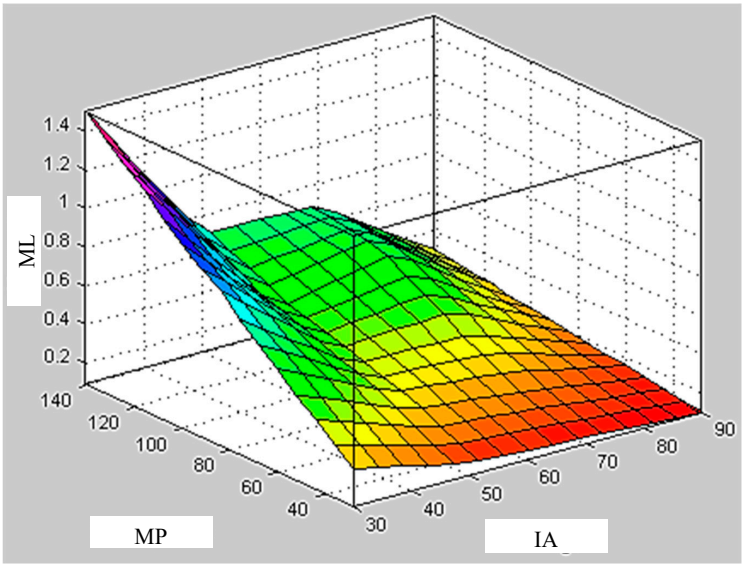

Figure 20. Mass loss (ML) in relation to change in slurry impact angle (IA) and mass of erodent (MP) using sea water.

It is important to acknowledge a methodological limitation regarding model validation. Due to the constrained dataset size (n = 20), the ANFIS model was developed using the complete dataset for training, without an independent hold-out test set or cross-validation procedure. While the experimental design (4 impact angles × 5 erodent masses × 2 media) captures the primary parameter space, and while the model shows an excellent fit to the experimental data, this approach does not constitute true predictive validation on unseen data.

The regression and ANOVA comparisons with ANFIS presented in Sections 3.5.1 and 3.5.2 confirm the statistical significance of the identified trends within the experimental domain, but they do not substitute for independent model validation. Therefore, the model's predictive generalization beyond the specific parameter ranges studied (impact angles 30–90°, erodent mass 28–141 g, constant slurry concentration, fixed impact velocity) should be interpreted with appropriate caution. The ANFIS model is best understood as an accurate interpolator within the experimental design space rather than a validated predictive tool for extrapolation to untested conditions.

4. Conclusions

This study investigated the slurry erosion behavior of as-built selective laser-melted (SLM) Ti-6Al-4V as a function of the erodent mass (MP) and impact angle (IA) in both pure water and saline environments. An adaptive neuro-fuzzy inference system (ANFIS) was developed to model and predict mass loss (ML), with its results showing a strong agreement with statistical regression and ANOVA.

The ANOVA analysis confirmed that ML is significantly and predictably influenced by media type, IA, and MP, with the model accounting for over 95% of the variance. The erodent mass was identified as the dominant factor, followed by IA and the media type. The experimental results further revealed that MP governs the extent of material loss, while IA dictates the erosion mode. The maximum mass loss occurred at a 30° impact angle and the minimum occurred at 90°, consistent with typical ductile erosion behavior, with the mass loss increasing nearly linearly with particle exposure across all angles.

The saline environment played a significant role, consistently enhancing the cumulative mass loss by approximately 16% compared to pure water under identical mechanical conditions. This indicates that the aqueous medium amplifies both the baseline degradation and the material's response to erodent mass.

The ANFIS model demonstrated an excellent predictive performance, evidenced by a high coefficient of determination ($R^2 > 0.95$) and low Root Mean Square Error (RMSE = 0.091). It effectively captured the nonlinear interactions among the erodent mass, impact angle, and environmental medium. The near-significant three-way interaction observed suggests complex underlying mechanisms that warrant further investigation. Overall, this validated framework provides a reliable computational tool for predicting the slurry erosion performance of SLM-fabricated Ti-6Al-4V under multi-parameter conditions, substantiating its practical application in material selection and design.

The primary contribution of this research lies in the convergence of three distinct elements: the investigation of a modern, additively manufactured material; the application of advanced computational modeling for a specific optimization goal; and the rigorous validation of this model against conventional statistical benchmarks. This study moves beyond prior erosion–corrosion research in the following key aspects:

While the erosion behavior of wrought Ti-6Al-4V is documented, its performance when produced via Selective Laser Melting (SLM) remains critically underexplored. This research provides the first systematic investigation into the synergistic effects of the slurry impact angle and erodent mass on the mass loss of SLM-manufactured Ti-6Al-4V.

The novelty is not in the use of ANFIS itself, but its strategic application to achieve a tangible engineering outcome. The model is employed to not only predict mass loss but, more importantly, to optimize the manufacturing and operational parameters (specifically medium type, impact angle, and erodent mass) to minimize material degradation. This transforms the work from a descriptive case study into a prescriptive tool, offering specific, data-driven recommendations for improving the durability of SLM-produced components.

To address the use of a smaller dataset and justify the neuro-fuzzy approach, the ANFIS model is not presented in isolation. Its performance is rigorously benchmarked against simpler, well-established statistical techniques, including Linear Regression, and validated using Analysis of Variance (ANOVA). This comparative framework quantitatively demonstrates that ANFIS captures complex, non-linear interactions between variables (interactions that simpler models fail to identify), leading to a superior predictive accuracy and providing a clear mathematical justification for its application.

While the ANFIS model demonstrates an excellent agreement with experimental measurements within the studied parameter space, a limitation of this work is the absence of independent validation on a hold-out test dataset, necessitated by the practical constraints of experimental data collection. Consequently, the model's predictive capability beyond the specific conditions investigated should be viewed with appropriate caution.

5. Limitations and Future Directions

The limitations of this study are: (1) only a single set of SLM processing parameters was employed; hence, the ANFIS model does not enable any assessment of the impact of Laser Power, Scan Speed or other process parameters on the slurry erosion–corrosion of Ti-6Al-4V alloys; (2) quantitative measurements of the porosity and relative density of the Ti-6Al-4V specimens produced using SLM were not investigated (the manufacturer-validated process parameter used yielded a near-full density product (99.8%) that can be used for structural purposes, but the density was not measured). A qualitative discussion of how the porosity may have affected crack initiation and propagation in erosion was not pursued. A third limitation is the qualitative treatment of the impact of the microstructure on erosion/corrosion resistance; yet another is that Powder Particle Size Distribution (PSD) was not measured independently of the test specimens, which may have obscured the effects of the SLM process and product density/microstructure that contribute to erosion/corrosion resistance. Future work will address these limitations by: (1) extending the ANFIS model to include all relevant SLM parameters, (2) collecting additional data at intermediate parameter combinations not used in training to serve as validation points, (3) acquiring a complete set of porosity measurements for the Ti-6Al-4V specimens, (4) establishing a quantitative relationship between the material microstructure and erosion/corrosion resistance, and (5) determining the impact of PSD on the slurry wear synergy by establishing flowability–density–corrosion correlations.

Author Contributions: Conceptualization, S.A.A., Y.A. and O.A.; methodology, I.M., Y.A. and O.A.; software, I.M.; validation, Y.A. and O.A.; formal analysis, I.M.; investigation, S.A.A.; resources, S.A.A.; data curation, O.A.; writing—original draft preparation, Y.A. and O.A.; writing—review and editing, S.A.A. and I.M.; visualization, O.A.; supervision, S.A.A.; project administration, S.A.A.; funding acquisition, S.A.A. All authors have read and agreed to the published version of the manuscript.

Funding: This research was funded by the Deanship of Postgraduate Studies and Scientific Research at Majmaah University through the project number (R-2026-92).

Data Availability Statement: The original contributions presented in this study are included in the article. Further inquiries can be directed to the corresponding authors.

Acknowledgments: The author extends appreciation to the Deanship of Postgraduate Studies and Scientific Research at Majmaah University for funding this research work through the project number (R-2026-92).

Conflicts of Interest: The authors declare no conflicts of interest.

References

1. Khayatan, N.; Ghasemi, H.M.; Abedini, M. Synergistic Erosion-Corrosion Behavior of Commercially Pure Titanium at Various Impingement Angles. *Wear* **2017**, *380–381*, 154–162. [CrossRef]
2. Chen, F.-J.; Yao, C.; Yang, Z.-G. Failure Analysis on Abnormal Wall Thinning of Heat-Transfer Titanium Tubes of Condensers in Nuclear Power Plant Part II: Erosion and Cavitation Corrosion. *Eng. Fail. Anal.* **2014**, *37*, 42–52. [CrossRef]
3. Kumar, N.; Shukla, M. Finite Element Analysis of Multi-Particle Impact on Erosion in Abrasive Water Jet Machining of Titanium Alloy. *J. Comput. Appl. Math.* **2012**, *236*, 4600–4610. [CrossRef]
4. Liu, Y.; Alfantazi, A.; Schaller, R.F.; Asselin, E. Localised Instability of Titanium during Its Erosion-Corrosion in Simulated Acidic Hydrometallurgical Slurries. *Corros. Sci.* **2020**, *174*, 108816. [CrossRef]
5. Bermúdez, M.-D.; Carrión, F.J.; Martínez-Nicolás, G.; López, R. Erosion–Corrosion of Stainless Steels, Titanium, Tantalum and Zirconium. *Wear* **2005**, *258*, 693–700. [CrossRef]
6. Singh, R. Integrity of Additively Manufactured Alloys and Component to Environmental Degradation. *J. Mater. Eng. Perform.* **2023**, *32*, 935–954. [CrossRef]
7. Baharzadeh, E.; Rafiei, M.; Mostaan, H.; Keshavarz, M.; Abazari, S.; Drelich, J.W.; Goldman, J.; Chen, X.; Motaharinia, A.; Bakhsheshi-Rad, H.R. Additive Manufacturing of Ti-Based Alloys: Microstructure, Mechanical Properties, and Corrosion Behavior. *J. Mater. Eng. Perform.* **2025**. [CrossRef]
8. García-Hernández, C.; García-Cabezón, C.; González-Diez, F.; Ampudia, M.; Juanes-Gusano, D.; Rodriguez-Cabello, J.C.; Martín-Pedrosa, F. Effect of Processing on Microstructure, Mechanical Properties, Corrosion and Biocompatibility of Additive Manufacturing Ti-6Al-4V Orthopaedic Implants. *Sci. Rep.* **2025**, *15*, 14087. [CrossRef]
9. Pal, S.; Velay, X.; Saleem, W. Investigation into the Electrochemical Corrosion Characteristics of As-Built SLM Ti-6Al-4 V Alloy in Electrolytic Environments. *J. Bio Tribocorros.* **2024**, *10*, 89. [CrossRef]
10. Liu, Z.; Zhang, L.; Ren, D.; Ma, A.; Ji, H.; Zheng, Y. Corrosion Behavior of Ti−6Al−4V Alloy Fabricated by Selective Laser Melting in Simulated Spent Fuel Reprocessing Environment. *Trans. Nonferrous Met. Soc. China* **2024**, *34*, 2167–2180. [CrossRef]
11. Chen, X.; Liao, Q.; Gong, M.; Fu, Q. Corrosion Performances of Selective Laser Melting Ti6Al4V Alloy in Different Solutions. *Metals* **2023**, *13*, 192. [CrossRef]
12. Fischer, D.; Cheng, K.; Neto, M.Q.; Hall, D.; Bijukumar, D.; Espinoza Orías, A.A.; Pourzal, R.; van Arkel, R.J.; Mathew, M.T. Corrosion Behavior of Selective Laser Melting (SLM) Manufactured Ti6Al4V Alloy in Saline and BCS Solution. *J. Bio- Tribo-Corros.* **2022**, *8*, 63. [CrossRef] [PubMed]
13. Huang, L.; Zheng, S.; Qin, Y.; Han, J.; Qiao, Y.; Chen, J. Corrosion Behavior of Selective Laser Melted Ti-6Al-4V in 0.1 Mol/L NaOH Solution. *Coatings* **2023**, *13*, 150. [CrossRef]
14. Sunitha, K.; Verma, P.; Vasudev, H.; Hua Yang, C. Fabrication of Metallic Materials for Erosion Resistance. In *Slurry Erosion: Flow Phenomenon, Complexities, and Protection Methods*; Singh, J., Kumar, S., Eds.; Kumar: Boca Raton, FL, USA, 2026; pp. 120–136.
15. Câmara Noronha, L.; Velho de Castro, V.; Ludwig, G.A.; Moreira Schroeder, R.; de Fraga Malfatti, C. Ti–Cp: Eletrochemical Behaviour Under Slurry Erosion Wear. *J. Bio- Tribo-Corros.* **2021**, *7*, 8. [CrossRef]
16. Qi, K.; Yang, Z.; Zhang, Y.; Li, G.; Li, K.; Yao, X.; Jiang, L. Magnetic Field-Assisted Laser Cladding of FeCoCrNiAl High-Entropy Alloy Coatings on Invar Steel Substrate. *JOM* **2025**. [CrossRef]
17. Li, D.; Ru, Y.; Chen, Z.; Dong, C.; Dong, Y.; Liu, J. Accelerating the Design and Development of Polymeric Materials via Deep Learning: Current Status and Future Challenges. *APL Mach. Learn.* **2023**, *1*, 021501. [CrossRef]
18. Sood, A.K.; Equbal, A.; Toppo, V.; Ohdar, R.K.; Mahapatra, S.S. An Investigation on Sliding Wear of FDM Built Parts. *CIRP J. Manuf. Sci. Technol.* **2012**, *5*, 48–54. [CrossRef]
19. Sai, T.; Pathak, V.K.; Srivastava, A.K. Modeling and Optimization of Fused Deposition Modeling (FDM) Process through Printing PLA Implants Using Adaptive Neuro-Fuzzy Inference System (ANFIS) Model and Whale Optimization Algorithm. *J. Braz. Soc. Mech. Sci. Eng.* **2020**, *42*, 617. [CrossRef]
20. Buj-Corral, I.; Sánchez-Casas, X.; Luis-Pérez, C.J. Analysis of Am Parameters on Surface Roughness Obtained in Pla Parts Printed with Fff Technology. *Polymers* **2021**, *13*, 2384. [CrossRef]

21. El Youbi El Idrissi, M.A.; Laaouina, L.; Jeghal, A.; Tairi, H.; Zaki, M. Application of Machine Learning in Fused Deposition Modeling: A Review. In *Proceedings of the Digital Technologies and Applications*; Motahhir, S., Bossoufi, B., Eds.; Springer Nature: Cham, Switzerland, 2023; pp. 114–124.
22. Rajesh, R.; Kulkarni, M.V.; Sampathkumaran, P.; Kumar, S.A.; Seetharamu, S.; Katiyar, J.K. Tribological Performance Involving DOE of an Additively Cu-Ni Alloy. In *Industrial Tribology*; Katiyar, J.K., Ruggiero, A., Rao, T.V.V.L.N., Davim, J.P., Eds.; CRC Press: Boca Raton, FL, USA, 2022; pp. 75–96, ISBN 9781003243205.
23. Shamshirband, S.; Malvandi, A.; Karimipour, A.; Goodarzi, M.; Afrand, M.; Petković, D.; Dahari, M.; Mahmoodian, N. Performance Investigation of Micro- and Nano-Sized Particle Erosion in a 90° Elbow Using an ANFIS Model. *Powder Technol.* **2015**, *284*, 336–343. [CrossRef]
24. Arunadevi, M.; Shivashankar, R.; Durga Prasad, C.; Baitha, R.; Suresh Kumar, R.; Choudhary, R.K.; Kollur, S.; Kapadani, K.R.; ShivaPrakash, S. Predictive Wear Analysis of SS316L Fabricated by Direct Energy Deposition Using Machine Learning Techniques. *Int. J. Interact. Des. Manuf. (IJIDeM)* **2024**. [CrossRef]
25. Sakthi Balan, G.; Aravind Raj, S.; Sridharan, M.; Adithya, R.N. A Study of the Effect of Printing Process Parameters on the Delamination and Surface Finish Properties of Aluminium-Infused PLA Printed via Material Extrusion. *Aust. J. Mech. Eng.* **2025**, *23*, 17–37. [CrossRef]
26. Wang, C.; Tan, X.P.; Tor, S.B.; Lim, C.S. Machine Learning in Additive Manufacturing: State-of-the-Art and Perspectives. *Addit. Manuf.* **2020**, *36*, 101538. [CrossRef]
27. Heshmat, M.; Maher, I.; Abdelrhman, Y. Surface Roughness Prediction of Polylactic Acid (PLA) Products Manufactured by 3D Printing and Post Processed Using a Slurry Impact Technique: ANFIS-Based Modeling. *Prog. Addit. Manuf.* **2023**, *8*, 87–98. [CrossRef]
28. Kosinska, A.; Balakin, B.V.; Kosinski, P. Theoretical Analysis of Erosion in Elbows Due to Flows with Nano- and Micro-Size Particles. *Powder Technol.* **2020**, *364*, 484–493. [CrossRef]
29. Ramesh, C.S.; Jain, V.K.S.; Keshavamurthy, R.; Khan, Z.A.; Hadfield, M. Prediction of Slurry Erosive Wear Behaviour of Al6061 Alloy Using a Fuzzy Logic Approach. In *Proceedings of the WIT Transactions on Engineering Sciences*; WIT Press: Southampton, UK, 2013; Volume 78, pp. 109–119.
30. Şahin, M.; Erol, R. A Comparative Study of Neural Networks and ANFIS for Forecasting Attendance Rate of Soccer Games. *Math. Comput. Appl.* **2017**, *22*, 43. [CrossRef]
31. Saleh, B.; Maher, I.; Abdelrhman, Y.; Heshmat, M.; Abdelaal, O. Adaptive Neuro-Fuzzy Inference System for Modelling the Effect of Slurry Impacts on PLA Material Processed by FDM. *Polymers* **2021**, *13*, 118. [CrossRef]
32. Aldahash, S.A.; Abdelaal, O.; Abdelrhman, Y. Slurry Erosion-Corrosion Characteristics of as-Built Ti-6Al-4V Manufactured by Selective Laser Melting. *Materials* **2020**, *13*, 3967. [CrossRef]
33. Peng, P.W.; Yang, J.C.; Lee, W.F.; Fang, C.Y.; Chang, C.M.; Chen, I.J.; Hsu, C.; Yang, T. Sen Effects of Heat Treatment of Selective Laser Melting Printed Ti-6al-4v Specimens on Surface Texture Parameters and Cell Attachment. *Appl. Sci.* **2021**, *11*, 2234. [CrossRef]
34. Abouel-Kasem, A.; Abd-elrhman, Y.M.; Emara, K.M.; Ahmed, S.M. Design and Performance of Slurry Erosion Tester. *J. Tribol.* **2010**, *132*, 021601. [CrossRef]
35. Fullér, R. *Neural Fuzzy Systems*; Åbo Akademi University: Åbo, Finland, 1995.
36. Foundations of Neural Networks, Fuzzy Systems, and Knowledge Engineering: Nikola K. Kasabov. MIT Press, Cambridge, MA. (1996). 550 Pages. $60.00. *Comput. Math. Appl.* **1997**, *33*, 136. [CrossRef]
37. Jang, J.S.R.; Sun, C.T.; Mizutani, E. *Neuro-Fuzzy and Soft Computing-A Computational Approach to Learning and Machine Intelligence*; Prentice-Hall: Hoboken, NJ, USA, 1997.
38. Kasperovich, G.; Hausmann, J. Improvement of Fatigue Resistance and Ductility of TiAl6V4 Processed by Selective Laser Melting. *J. Mater. Process. Technol.* **2015**, *220*, 202–214. [CrossRef]
39. Jeyaprakash, N.; Yang, C.H.; Prabu, G.; Radhika, N. Mechanism Correlating Microstructure and Wear Behaviour of Ti-6Al-4V Plate Produced Using Selective Laser Melting. *Metals* **2023**, *13*, 575. [CrossRef]
40. Ahn, B. Microstructural Tailoring and Enhancement in Compressive Properties of Additive Manufactured Ti-6al-4v Alloy through Heat Treatment. *Materials* **2021**, *14*, 5524. [CrossRef] [PubMed]
41. Murr, L.E.; Quinones, S.A.; Gaytan, S.M.; Lopez, M.I.; Rodela, A.; Martinez, E.Y.; Hernandez, D.H.; Martinez, E.; Medina, F.; Wicker, R.B. Microstructure and Mechanical Behavior of Ti–6Al–4V Produced by Rapid-Layer Manufacturing, for Biomedical Applications. *J. Mech. Behav. Biomed. Mater.* **2009**, *2*, 20–32. [CrossRef]
42. Finnie, I.; Stevick, G.R.; Ridgely, J.R. The Influence of Impingement Angle on the Erosion of Ductile Metals by Angular Abrasive Particles. *Wear* **1992**, *152*, 91–98. [CrossRef]
43. Abdelrhman, Y.; Abouel-Kasem, A.; Emara, K.; Ahmed, S. The Effect of Boronizing Heat Treatment on the Slurry Erosion of AISI 5117. *Ind. Lubr. Tribol.* **2018**, *70*, 1176–1186. [CrossRef]

44. Abd-Elrhman, Y.M.; Abouel-Kasem, A.; Emara, K.M.; Ahmed, S.M. Effect of Impact Angle on Slurry Erosion Behavior and Mechanisms of Carburized AISI 5117 Steel. *J. Tribol.* **2013**, *136*, 011106. [CrossRef]
45. Saleh, B.; Ahmed, S.M. Slurry Erosion–Corrosion of Carburized AISI 5117 Steel. *Tribol. Lett.* **2013**, *51*, 135–142. [CrossRef]

Disclaimer/Publisher's Note: The statements, opinions and data contained in all publications are solely those of the individual author(s) and contributor(s) and not of MDPI and/or the editor(s). MDPI and/or the editor(s) disclaim responsibility for any injury to people or property resulting from any ideas, methods, instructions or products referred to in the content.